Effects of realistic laser intensity and phase distribution on high-charge laser wakefield acceleration

Yuhui Xia,[1] Zhenan Wang,[1] Ziyao Tang,[1] Jianghao Hu,[1] Qianyi Ma,[1] Yuekai Chen,[1] Letian Liu,[1] Zhiyan Yang,[1] Hui Zhang,[1] Chenxu Wang,[1] Haoyang Lan,[1,2] Di Wu,[1,2] Xiuhong Yang,[1,2] Yixing Geng,[1,2] Yanying Zhao,[1,2,*] Xueqing Yan,[1,2,3] and Xinlu Xu[1,2,†]

[1]*State Key Laboratory of Nuclear Physics and Technology, and Key Laboratory of HEDP of the Ministry of Education, CAPT, Peking University, Beijing 100871, China*

[2]*Beijing Laser Acceleration Innovation Center, Beijing 100871, China*

[3]*Institute of Guangdong Laser Plasma Technology, Baiyun, Guangzhou, 510540, China*

(Received 9 November 2025; accepted 2 April 2026; published 13 May 2026)

Laser wakefield acceleration (LWFA) can produce relativistic electron beams and various secondary particles in centimeter-long plasmas, making it a valuable particle source with important applications in many disciplines. In this work, we examine the effects of nonideal transverse intensity and phase distribution of laser pulses on LWFA through both experimental measurements and particle-in-cell simulations. The complex transverse profile of the 75 TW laser pulses reduces the self-focused intensity in the plasma compared with a transversely Gaussian laser pulse. Furthermore, the sheath structure of the nonlinear plasma wake excited by realistic laser pulses is wider and more complicated than that of a Gaussian laser pulse. These features hinder electron injection. As the laser pulse propagates through the plasma, its intensity profile gradually becomes elliptical and drives a plasma wake with a sharp sheath near the azimuths of the major axis, leading to electron injection. When using a realistic laser profile in simulations, both the charge and energy of injected electrons closely match experimental results (∼200 pC of charge and ∼200 MeV peak energy), whereas the Gaussian laser simulations produce much higher charge (∼500 pC). Our findings reveal differences in injection dynamics between LWFA driven by nonideal laser pulses and those driven by Gaussian pulses and are useful for applications of LWFA that demand high-charge electron beams.

DOI: 10.1103/cgc6-75tf

I. INTRODUCTION

Laser wakefield acceleration (LWFA) [1] can generate monoenergetic electron beams with hundreds of MeV to ∼10 GeV energies [2–8], ∼femtosecond durations [9–14], and ∼mrad divergences [15–17] in centimeter-long plasmas [18,19]. As compact and economical sources of relativistic electrons, LWFA holds significant potential for applications in fields ranging from next-generation colliders to compact x-ray free-electron lasers [20–22]. Meanwhile, ultrafast secondary x-ray and γ-ray radiation produced through betatron radiation [23], Compton scattering [24,25], and bremsstrahlung based on LWFA have been applied in x-ray phase contrast imaging [26], microcomputed tomography [27], x-ray absorption spectroscopy [28], and photonuclear reactions [29], exhibiting advantages in compactness, collimation, ultrashort duration, and brightness. These applications, which benefit from a large number of photons, usually demand high charge relativistic electron beams while having loose requirements on beam quality (energy spread and emittance) [30]. Various schemes have been explored experimentally to improve the injected charge. Several hundred pC monoenergetic electron beams with ∼100 MeV energy have been generated using widespread 100-TW, joule-level laser systems through self-injection [31,32], ionization injection [33], density downramp injection [34,35], and nanoparticle-insertion scheme [36].

In most studies on LWFA, the laser pulse driver is assumed to have a diffraction-limit Gaussian transverse profile. However, realistic laser pulses delivered by state-of-the-art ultrafast high-power laser systems often deviate from the ideal Gaussian beam in both intensity and phase due to complex amplification and compression procedures [37–39]. During the rapid development of LWFA over the past decade, researchers have increasingly focused on the fine dynamics of the evolution of laser pulses in plasmas, the injection and acceleration of electrons, and the reproducibility of LWFA [40–43]. Consequently, the imperfections of realistic laser

*Contact author: zhaoyanying@pku.edu.cn
†Contact author: xuxinlu@pku.edu.cn

Published by the American Physical Society under the terms of the Creative Commons Attribution 4.0 International license. Further distribution of this work must maintain attribution to the author(s) and the published article's title, journal citation, and DOI.

pulses and their impact on LWFA have become increasingly significant. Previous studies have shown that a laser pulse with an imperfect wavefront [44,45] or intensity distribution [46–48] drives an inhomogeneous transverse wakefield, which affects the transverse distribution of the electrons. Additionally, non-Gaussian lasers have been found to strongly degrade the betatron x-ray emission [49]. Recent works have demonstrated that a specific complex wavefront improves the performance of LWFA [50,51].

In this paper, we combine experiments and particle-in-cell (PIC) simulations to demonstrate that imperfections in a realistic laser pulse substantially reduce the injected electron charge. A 35 fs Ti:Sapphire laser pulse with a 1.3 J energy is incident on a helium gas jet and produces electrons with a peak energy of ∼200 MeV and a total charge of ∼200 pC. The charge is significantly lower than PIC simulation results using a transversely Gaussian laser with the same peak power. By importing the realistic laser distribution reconstructed using the Gerchberg-Saxton (GS) algorithm into the PIC simulation, we find that nonideal intensity and phase distributions of the laser lower the self-focused laser intensity, blur the sheath structure of the nonlinear plasma wake, and hinder electron injection at the initial stage of plasma evolution. As the relativistic laser pulse propagates through the plasma, its intensity profile evolves into an ellipse and enables electron injection. The charge and energy of the injected electrons in simulations using realistic laser pulse agree well with experiments. In Sec. II, we present the experimental results of the LWFA. In Sec. III, a comparison is performed between PIC simulations of LWFA driven by a Gaussian laser pulse, an elliptical laser pulse and a reconstructed realistic laser pulse, and the differences in laser pulse evolution, plasma wake excitation, and electron injection are discussed. A summary of our finding is given in Sec. IV.

II. EXPERIMENTAL SETUP AND RESULTS

A schematic of the experiment is shown in Fig. 1(a). The experiment was carried out at the Compact Laser Plasma Accelerator Laboratory (CLAPA) at Peking University, utilizing a 5 Hz high power Ti:sapphire laser system. A x direction (horizontally) linearly polarized laser pulse had a full width at half maximum (FWHM) pulse duration of 35 fs and was focused down to a spot size of $w_0 \approx 25.9$ μm via an F/12.5 off-axis parabolic mirror. A typical spatial intensity distribution of the laser focal spot is shown in the inset of Fig. 1(a). The laser energy within the $1/e^2$ radius was 1.3 J, accounting for 51% of the total energy. This corresponds to a peak normalized vector potential $a_0 \equiv \frac{eE_0}{mc\omega_0} \approx 1.44$, where E_0 and ω_0 are the electric field and the frequency of the laser, m and e are the electron mass and charge, and c is the speed of light in vacuum. A 4-mm-long and 1-mm-wide De Laval supersonic gas nozzle provided a helium gas target. A probe laser beam [not shown in Fig. 1(a)], perpendicular to the main laser propagation axis and containing 2% energy of the main pulse, was used to diagnose the plasma density in a Michelson interferometer. A typical plasma electron density distribution at a height of 2 mm above the nozzle when the backing pressure was 21 bar is presented in Fig. 1(b), and the red line shows the on-axis density profile. The plasma density had an approximately linear dependence on the backing pressure, as shown in Fig. 1(c).

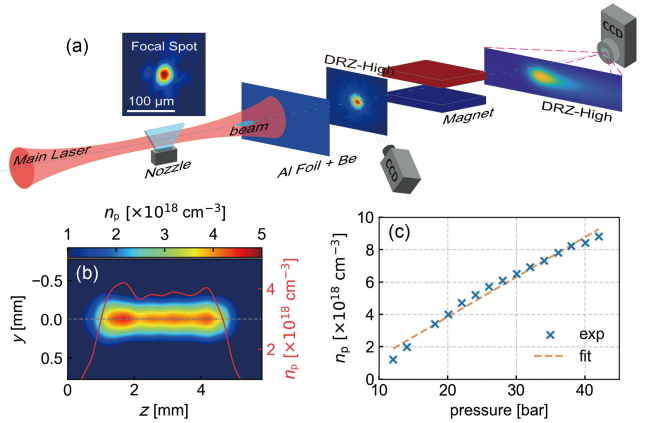


FIG. 1. (a) Schematic of the experimental setup (not to scale). The inset shows a typical spatial intensity distribution of the laser focal spot. A 10 μm thick aluminum film is placed near the gas nozzle to block the laser pulse while allowing relativistic electrons to pass through it with minimal impact. (b) A typical plasma electron density distribution measured by the Michelson interferometer and the axial plasma density profile (red line). (c) The dependence of the plasma density on the backing pressure. The plasma density is measured at a height of 2 mm above the nozzle.

A 20 × 23 cm dipole magnet with a 0.8 T peak magnetic field was placed 80 cm away from the gas nozzle to measure the beam energy spectrum with a reliable energy range of 70 to 350 MeV. Two GOS (Gd_2O_2S: Tb, $\rho_{GOS} = 7.44$ g/cm^3) scintillators (DRZ-High, phosphor surface loading of 145 mg/cm^2) were individually positioned at the entrance and the exit of the magnet. Two imaging systems with Andor CCD recorded the divergence and the pointing angle of the electron beams at the first screen and the energy spectrum at the second screen. The beam charge was calculated using the measured signals at the second screen by taking into account the photon generation and transmission efficiencies from the scintillator to the CCD. The scintillator was calibrated with a conventional electron accelerator.

Pure helium gas was used and we relied on the evolution of the laser pulse driver to trap electrons [2–4,52,53]. For the interaction between an ultrashort and ultraintense laser pulse and an underdense plasma, self-focusing, self-phase modulation, and pump depletion occur [54], and the laser pulse and the excited plasma wake evolve significantly. When the laser peak intensity is high and the wake expands

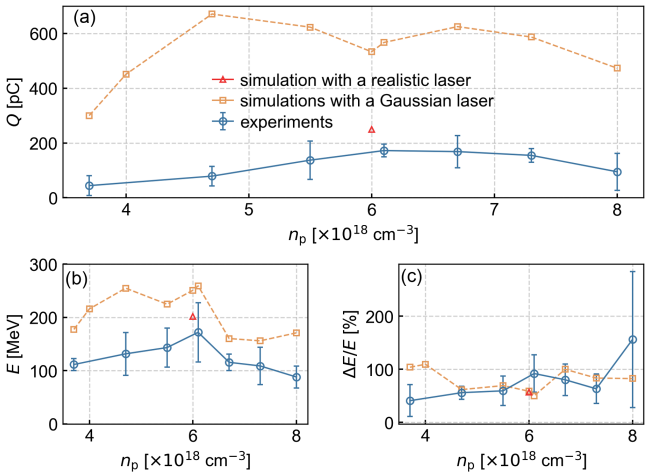


FIG. 2. Experimental results of the injected electron beams when scanning the plasma density n_p. The dependence of the injected charge (a), the peak energy (b), and the relative FWHM energy spread on n_p. Note z_f is fixed as -1 mm in these experiments. The presented results are averaged over 5–15 shots at each n_p. The orange squares show the PIC simulation results when using a transversely Gaussian laser pulse driver and the red triangle shows the result with a reconstructed laser pulse.

(i.e., the phase velocity of the wake tail is significantly less than the speed of light), some sheath electrons of the nonlinear plasma wake with high forward velocities can be trapped and accelerated to hundreds of MeV energy. In the experiments, the relative position between the laser focal plane and the gas nozzle and the plasma density were examined to optimize the charge of the injected beams. We moved the gas nozzle along the laser propagation path to scan the relative focal position from $z_f = -2.4$ to 0.4 mm and found that the injected charge does not exhibit a strong dependence on z_f. Here $z_f = 0$ mm indicates the laser is focused at the middle of the gas nozzle. This may be due to the long vacuum Rayleigh length of the laser we used, $z_R \approx 2.6$ mm. We fixed the relative focal position as $z_f = -1$ mm in the subsequent experiments.

The plasma density n_p plays a critical role in the laser pulse evolution and the injection of electrons. We scanned the plasma density by changing the backing pressure of the nozzle. The measured beam charge under different n_p is depicted in Fig. 2(a). When $n_p < 3 \times 10^{18}$ cm^{-3}, the self-focusing of the laser pulse is weak, and its peak a_0 is less than 3.5 as revealed in PIC simulations using transversely Gaussian laser pulses, resulting in no detectable experimental signal in the screen. The injected charge increased from 44 to 172 pC as the density increased from 3.7×10^{18} to 6.1×10^{18} cm^{-3}. The injected charge reached its maximum when $n_p = 6.1 \times 10^{18}$ cm^{-3} and then decreased as the density continued to increase. For high density plasmas, the injected electrons are decelerated at the tail of the plasma due to the strong pump depletion of the laser pulse and the dephasing [35], resulting in a reduction in the measured charge which only counts electrons with ≥ 70 MeV energy.

The peak energy of the electron beams is shown in Fig. 2(b). As n_p increased from 3.7×10^{18} to 6.1×10^{18} cm^{-3}, the beam energy also increased. This is probably caused by an increasing axial plasma wakefield ($E_z \propto \sqrt{n_p}$) and fixed plasma length. After $n_p = 6.1 \times 10^{18}$ cm^{-3}, the energy decreased as n_p increased, which is due to the dephasing between the electrons and the laser driver [55]. The relative FWHM (full width at half maximum) energy spread of the beams was large, ~100%, as shown in Fig. 2(c).

PIC simulations employing laser pulses with transversely Gaussian profiles reveal electron injection with significantly higher charge than observed in experimental measurements [orange squares in Fig. 2(a)]. For example, the injected charge when $n_p = 6 \times 10^{18}$ cm^{-3} is 533 pC in simulations and 172 pC in experiments. This discrepancy may be caused by the imperfection of the transverse distribution of the realistic laser.

III. EFFECTS OF REALISTIC LASER INTENSITY AND PHASE DISTRIBUTION ON INJECTION

In the experiments, we measured the intensity profiles of the laser pulse at two planes along the propagation axis and retrieved the phase distribution utilizing the GS algorithm. Note that this phase retrieval algorithm is based on the time-integrated intensity profiles and thus cannot resolve the wavelength-dependent information. Details on how to get the three-dimensional (3D) field distribution of the laser pulse can be found in the Appendixes A and B. We then imported the realistic field distribution of the laser into quasithree-dimensional (Q3D) version [56] of the particle-in-cell (PIC) code OSIRIS [57] to study its driven LWFA. The simulation used a moving window with a box size of $706.8k_0^{-1}$ and $684k_0^{-1}$ and 3534×684 cells along the z and r directions, respectively, where $k_0 = \frac{2\pi}{0.8}$ μm^{-1} is the laser wave number. The grid sizes were $\Delta z = \frac{1}{5}k_0^{-1}$ (0.025 μm) and $\Delta r = k_0^{-1}$ (0.127 μm) < 0.44 μm (the spatial resolution of the laser spot diagnostic system). The time step $\Delta t = 0.1\omega_0^{-1}$ satisfied the Courant-Friedrichs-Lewy condition. Azimuthal modes from $m = 0$ to 6 were used and 48 macroparticles per cell were initialized to represent the plasma electrons for the realistic laser case. The realistic laser pulse (labeled as "case r") had $1/e^2$ radii of $w_x = 22.4$ μm (polarized direction) and $w_y = 29.3$ μm (orthogonal direction) and was focused at 1.2 mm downstream ($z_f = -1$ mm) from the plasma entrance with a peak $a_0 = 1.44$. If we fit the intensity profile at the focus with an ellipse, its major axis was inclined at 65.7° to the x axis. The Zernike coefficients of the realistic laser are shown in Fig. 9 in the Appendix A.

For comparison purposes, an additional Q3D simulation with 2 azimuthal modes ($m = 0, 1$) was performed using an ideal Gaussian laser pulse (labeled as "case g"). The spot

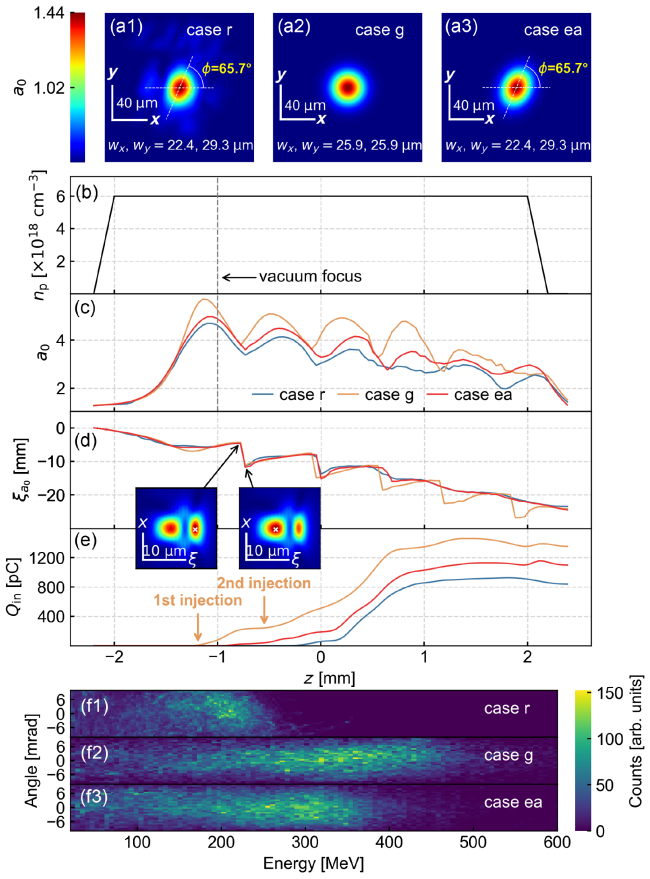


FIG. 3. (a1)–(a3) The transverse intensity distribution of the lasers at the vacuum focus. (b) The plasma density profile. The black dashed line indicates the vacuum focal plane. The evolution of a_0 (c) and their axial locations ξ_{a_0} (d) for three cases. The two insets show the $\xi - x$ intensity profile of the Gaussian laser at different propagation distances, with white crosses marking the locations of the intensity peaks. (e) The evolution of the injected charge for three cases. (f1)–(f3) The energy spectra of the injected beam at the plasma exit for three cases.

size of the Gaussian laser was $w_x = w_y = 25.9$ μm. To isolate the physical processes related to an elliptical laser intensity distribution, we also performed another simulation with 4 azimuthal modes using a laser pulse whose intensity profile was derived from the elliptical fit of the realistic laser (labeled as "case ea"). It also had the same astigmatism terms as the realistic laser, i.e., the Zernike coefficients $Z_2^{-2} = 0.745$ rad and $Z_2^2 = 0.656$ rad, resulting in a 1.09 mm separation between the tangential focus and the sagittal focus. This allowed us to specifically investigate the effect of nonaxisymmetric features of the laser driver on the electron injection in LWFA. Figures 3(a1)–3(a3) show the peak intensity profiles of these three lasers at the vacuum focus. The lasers have the same peak $a_0 = 1.44$ at the vacuum focus and the same Gaussian temporal envelope with a FWHM duration of 35 fs.

As shown by the black line in Fig. 3(b), a preionized plasma with $n_p = 6 \times 10^{18}$ cm^{-3}, featuring a 200- μm-long linear upramp, a 4-mm-long plateau, and a 200- μm-long linear downramp, was used in the simulations. Figure 3(c) shows the evolution of the peak a_0 for three cases. Since the laser peak power is ∼75 TW (on target), much higher than the self-focusing critical power ($P_c \approx 17 \frac{\omega_0^2}{\omega_p^2}$ GW ≈ 4.9 TW for $n_p = 6 \times 10^{18}$ cm^3 and 800 nm laser wavelength) [58,59], the laser pulse is self-focused by the plasma. The peak a_0 of the laser increases as the laser propagates inside the plasma and reaches its maximum value at $z \approx -1.1$ mm (before the vacuum focus $z_f = -1$ mm). The maximum a_0 for the Gaussian laser case is 5.7, significantly higher than the vacuum focused value ($a_0 = 1.44$). The elliptical laser and realistic laser cases exhibit lower maximum a_0 values of 5.0 and 4.7, respectively. As the laser pulse propagates further inside the plasma, the mutual interaction of the self-focusing and the diffraction results in an oscillation of a_0 with a decreasing amplitude. The oscillation period is ∼0.64 mm.

The temporal envelope of the laser evolves under rich laser-plasma interactions, e.g., the self-steepening, the self-phase modulation, and the group velocity dispersion [54]. As shown in the left inset in Fig. 3(d), the initial Gaussian temporal envelope with a duration of 35 fs gradually splits into two pulses at $z \approx -0.9$ mm [52]. At the moment of split, the a_0 of the preceding pulse is higher than that of the succeeding pulse. As the preceding pulse depletes its energy into the plasma and diffracts, the intensity of the succeeding pulse gradually surpasses it [the right inset of Fig. 3(d)]. This causes a steplike jump in the axial position where the peak a_0 is located (ξ_{a_0}, indicated by the white crosses in the insets), as shown in Fig. 3(d). Here $\xi \equiv ct - z$ is introduced to express the axial location in a frame moving at the speed of light. When the energy of the preceding pulse is nearly exhausted, the succeeding pulse repeats the split and causes the second jump of ξ_{a_0} at $z \approx 0$ mm. This process repeats more times for the Gaussian laser case than the other cases.

Figure 3(e) depicts different injection dynamics for three cases. In case g, the first injection occurs in -1.2 mm $< z < -0.8$ mm, where a_0 reaches its peak ($a_0 = 5.7$). Electrons with ∼200 pC charge are injected and form a short beam with a peak current of ∼30 kA. The second injection occurs at $z \approx -0.4$ mm and continues until $z \approx 0.7$ mm. In contrast, there is no injection when the a_0 reaches its maximum ($z \approx -1.1$ mm) for the elliptical laser and realistic laser cases. There is an injection of 184 pC charge between $z \approx -0.9$ mm and $z \approx 0$ mm for the elliptical laser case while the injected charge is only 49 pC for the realistic laser case. A significant injection happens between $z \approx 0.1$ mm and $z \approx 0.9$ mm for these two cases. At the plasma exit, the injected charge is 1.35 nC for the Gaussian laser case, 1.1 nC for the elliptical laser case, and 0.84 nC for the realistic laser case. To compare with the experimental results, which only counted electrons with energy above

70 MeV and divergence below 10 mrad, we selected electrons from simulations using the same criteria, and the results were 533 pC in case g, 417 pC in case ea, and 249 pC in case r. Recall that the experimental result at this plasma density and the vacuum focal position was 172 ± 23 pC, which agrees with the simulation using a realistic laser pulse. Figures 3(f1)–3(f3) show the electron energy spectra at the plasma exit. The peak energies are 251, 232, and 202 MeV for case g, ea, and r, respectively, which all agree reasonably with the experimental result (172 ± 56 MeV).

A close investigation of the nonlinear plasma wake was conducted to understand the different injection dynamics when using lasers with different spatiotemporal distribution. Since a preionized plasma is used in the simulations and there is no density downramp (except the plasma exit), the injection relies on the evolution of the laser pulse [2–4,52,53]. As the laser driver undergoes focusing [60] or diffraction [61], it may induce an expansion of the wake, consequently reducing the velocity of the wake tail. When the electrons in the high-density sheath surrounding the nonlinear plasma wake move to the wake tail, they can be injected if they are faster than the wake tail [60,62]. Figure 4(a) shows the evolution of $\frac{d\xi_t}{dz}$ for three cases, where ξ_t is defined as the axial location of the tail of the first wake. The black dashed line in 4(a) is the etching velocity of the laser driver in the 3D nonlinear regime ($v_{\text{etch}} \approx \frac{3}{2}\frac{\omega_p^2}{\omega_0^2} c \approx 0.0052c$) [55]. Due to the evolution of the laser spot size and the a_0, $\frac{d\xi_t}{dz}$ deviates from $-\frac{v_{\text{etch}}}{c}$. For case g, $\frac{d\xi_t}{dz}$ reaches its minimum (-0.016) at $z \approx -1.1$ mm where the laser reaches its maximum a_0, and induces an injection. The injection then ceases as a result of three synergistic effects: the decrease of a_0 [Fig. 3(c)], the increase of $\frac{d\xi_t}{dz}$ [Fig. 4(a)], and the beam loading effect from the ~30 kA injected beam. At $z \approx -0.4$ mm, $\frac{d\xi_t}{dz}$ decreases to -0.013 and remains relatively low for a long distance, resulting in the second injection from $z \approx -0.4$ mm to $z \approx 0.7$ mm.

For the elliptical laser case and the realistic laser case, $\frac{d\xi_t}{dz}$ reaches its minimum (-0.011) at $z \approx -1$ mm, slightly behind the location where the laser reaches its maximum a_0. However, the injection around this position is much weaker than the Gaussian laser case, as shown in Fig. 3(e). We show the transverse intensity distribution of the ξ_{a_0}-slice of the three laser pulses when they achieve the maximum a_0 in Figs. 4(b1)–4(b3) and the corresponding plasma density distribution at the central slice of the nonlinear wake in Figs. 4(c1)–4(c3). Here the central slice of the nonlinear wake is defined as the slice where the on-axis $E_z = 0$. The Gaussian laser pulse has an axisymmetrical intensity profile [Fig. 4(b2)] and the sheath structure of its excited nonlinear wake is axisymmetric and sharp [(c2)]. The intensity profile of the elliptical laser

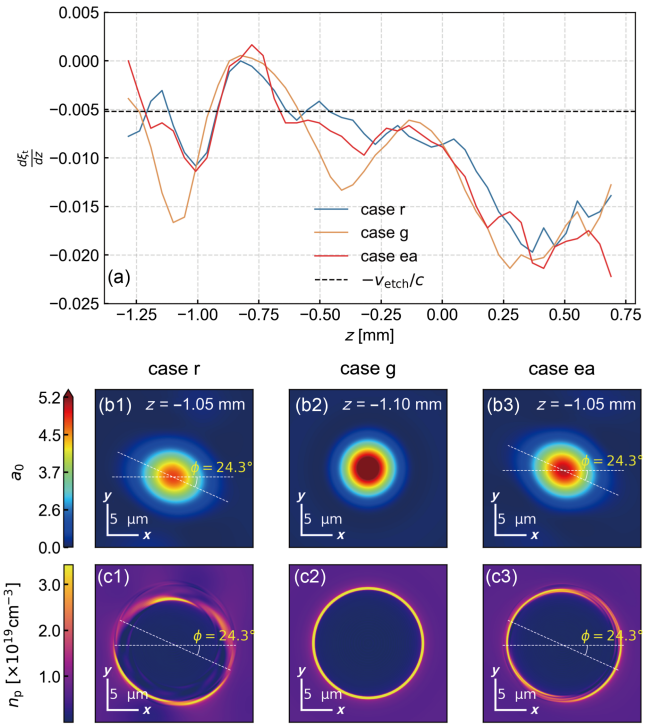


FIG. 4. (a) The evolution of $\frac{d\xi_t}{dz}$ for three cases. The black dashed lines are the theoretical value of $-\frac{v_{\text{etch}}}{c}$. (b1)–(b3) The transverse intensity profile of the ξ_{a_0}-slice of the lasers at the propagation distances where they achieve the maximum a_0. (c1)–(c3) The plasma density distribution at the central slice of the corresponding nonlinear wakes. The white dashed lines in (b1), (b3), (c1), (c3) represent the major axis of the laser transverse intensity profile and the x axis.

is shown in Fig. 4(b3). Due to the astigmatism, its major and minor axes have swapped relative to the initial state. As shown in Fig. 4(c3), a sharp and high-density sheath only exists along the major axis of the elliptical laser while the sheath becomes wide and complicated along the minor axis. Correspondingly, the forward velocity of the sheath electrons when they reside at the wake tail depends on their azimuthal angles. The electrons at the angles of the laser major axis have similar forward velocities comparable to the Gaussian case while electrons at other angles exhibit smaller forward velocities [63], which reduces the injected charge.

The evolution of the realistic laser and its excited nonlinear wake are more complicated than the elliptical laser case. As shown in Fig. 4(c1), the overall sheath structure exhibits a larger width than that in the elliptical case. Especially, the sheath structure at the angles of the laser major axis is wide and diffuse. This significantly reduces the forward velocity of the sheath electrons [64] and suppresses the injection at $z \approx -1$ mm, where $\frac{d\xi_t}{dz}$ reaches a local minimum. As the realistic laser propagates inside the plasma, the complex spatial features beyond an ellipse dissipate gradually [65] and its transverse intensity

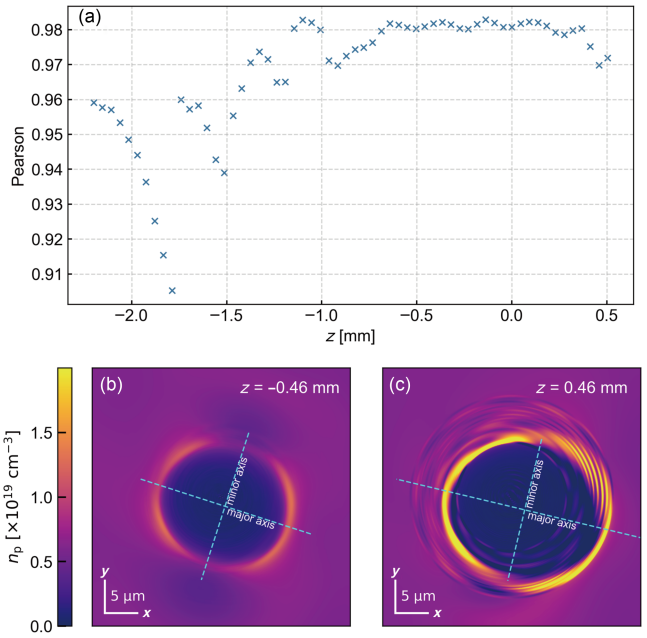


FIG. 5. (a) The Pearson correlation coefficient between the realistic laser profile and its elliptical fit. The plasma density distribution at the central slice of the nonlinear wakes for the realistic laser pulse at $z = -0.46$ mm (b) and $z = 0.46$ mm (c). The dashed lines represent the major and minor axes of the laser driver.

distribution is closer to an ellipse, as shown in Fig. 5(a), where the Pearson correlation coefficient is the covariance between the intensities of the realistic laser profile and the fitted elliptical profile, normalized by the product of their standard deviations [66]. A value of the Pearson correlation coefficient close to 1 indicates strong agreement between the realistic and fitted profiles. It is observed that at $z \approx -0.6$ mm, the realistic laser evolves into a well-defined elliptical laser, and propagates with an elliptical intensity profile in the plasma. Figures 5(b) and 5(c) show the sheath structure at two different propagation distances. At $z = -0.46$ mm, the sheath width at the laser major axis is narrower than that at the minor axis. However, the wake radius at this distance is small and the phase velocity of the wake tail is close to c [Fig. 4(a)], thus there is still no injection at this position. At $z = 0.46$ mm, the wake radius grows, a narrow and high-density sheath is formed at the laser major axis, and the tail phase velocity is low. The combined effect of these three factors results in the significant injection as shown in Fig. 3(e).

Simulations indicate that the non-Gaussian transverse distribution of the laser pulse reduces the maximum self-focused intensity in an underdense plasma. The a_0 evolution for the realistic laser and the elliptical laser is similar, which suggests that the self-focusing of our laser pulses is mainly determined by the transversely elliptical intensity distribution. Meanwhile, due to the lack of symmetry in the realistic laser intensity and phase profile, the sheath structure of its excited nonlinear plasma wake is wider and more complicated than that of the Gaussian laser case, which usually reduces the forward velocity of the sheath electrons and impedes injection. As a result, the injected charge decreases progressively from the Gaussian laser case to the elliptical laser case to the realistic laser case, with the latter aligning with the experimental results.

IV. CONCLUSION

In conclusion, we conducted LWFA experiments aiming to produce relativistic electron beams with high charge. By applying the GS algorithm, we reconstructed the wavefront of a realistic laser pulse and imported the field distribution into the Q3D PIC simulations. By comparing laser evolution, nonlinear plasma wake excitation, and injection in three cases—a Gaussian laser pulse, an elliptical laser pulse, and a reconstructed realistic laser pulse—we conclude that the realistic laser distribution hinders injection by lowering the self-focused intensity and blurring the sheath structure of the nonlinear wake. As the realistic laser pulse propagates in the plasma, its intensity distribution becomes close to an ellipse, which enables the injection. The simulation results of the injected charge when using the realistic laser pulse agree well with the experiments. This work indicates the importance of the optimization of the laser distribution when conducting LWFA experiments.

ACKNOWLEDGMENTS

We would like to thank Xuezhi Wu for helpful discussions. This work was supported by the Fundamental and Interdisciplinary Disciplines Breakthrough Plan of the Ministry of Education of China-JYB2025XDXM204, the National Grand Instrument Project No. SQ2019YFF01014400, Beijing outstanding young scientist project, National Natural Science Foundation of China No. 12375147, and the Fundamental Research Funds for the Central Universities, Peking University. The simulations were supported by the High-performance Computing Platform of Peking University.

DATA AVAILABILITY

The data that support the findings of this article are openly available [67], embargo periods may apply.

APPENDIX A: PHASE RETRIEVAL USING THE GS ALGORITHM

We measured the intensity profiles of the laser pulse using a Spiricon CCD SP620U, with an ×10 apochromatic (APO) objective lens. Figures 6(a) and 6(b) show the measured intensity profiles at the focus and at a plane located 1 mm upstream of the focus (labeled as "−1 mm"). By setting the intensity profiles as constraints and initializing the phase distribution following Refs. [68,69], the

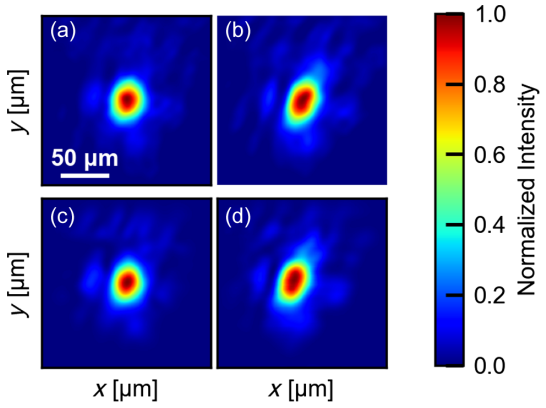


FIG. 6. GSA-MD results of the realistic laser pulse. (a) and (b) depict the measured intensity profiles at 0 and −1 mm, respectively. (c) and (d) are the retrieved intensity profiles at 0 and −1 mm, respectively. Note that a pixel in these plots represents a physical size of 0.44 × 0.44 μm.

phase distribution at the focal plane (far field) was retrieved after several thousand iterations. The phase retrieval algorithm implemented in this study is based on the GSA-MD algorithm [68,69], which decomposes the electromagnetic (EM) fields into Hermite-Gaussian modes, thereby ensuring the correctness of laser propagation. The retrieved phase was validated through a back-propagation test. By using the retrieved far-field intensity [Fig. 6(c)] and the retrieved phase, we calculated the intensity profile of a near-field plane ($z = -1$ mm) via angular spectrum (AS) diffraction code. Good agreement was achieved between the calculated near-field profile [Fig. 6(d)] and the measured one [Fig. 6(b)], which exhibits a structural similarity (SSIM) of 0.93 [70] and a peak signal-to-noise ratio (PSNR) of 37.5 dB in the image region [71]. Note that a higher SSIM (closer to 1) and a larger PSNR indicate better retrieved performance.

A detailed description of the GSA-MD algorithm is provided below. We defined the error function χ^2 and the gradient χ^2_{gradient} to quantify the reconstruction performance and the stop criterion as the Refs. [68,69],

$$\chi^2 = \sum_{\mathrm{k}=0}^{N_{\mathrm{i}}-1} \frac{\sqrt{\sum_{i=1}^{N_{\mathrm{p,x}}\times N_{\mathrm{p,y}}} [F_{\mathrm{exp}}(x,y,z_{\mathrm{k}}) - F_{\mathrm{fit}}(x,y,z_{\mathrm{k}})]^2}}{N_{\mathrm{i}} \sum_{i=1}^{N_{\mathrm{p,x}}\times N_{\mathrm{p,y}}} F_{\mathrm{exp}}(x,y,z_{\mathrm{k}})}, \tag{A1}$$

$$\chi^2_{\text{gradient}} = \frac{|\chi^2(\text{iter}) - \chi^2(\text{iter}-5)|}{\chi^2(\text{iter}-5)}, \tag{A2}$$

where N_{i} denotes the number of intensity planes employed in the GSA-MD, and $N_{\mathrm{p,x}} \times N_{\mathrm{p,y}}$ represents the number of transverse pixels. Here, F_{exp} and F_{fit} correspond to the intensity profiles measured in the experiment and reconstructed by the GSA-MD at the longitudinal position z_{k} (relative to the focus plane), respectively, with "iter" denoting the iteration number.

The convergence criteria for the GSA-MD are strictly set to $\chi^2 \le 0.002$ or $\chi^2_{\text{gradient}} \le 0.02$, with a maximum cap of 50 iterations, based on the recommendation of Ref. [69]. Typically, the algorithm achieves convergence within 30–50 iterations. However, in order to find the transverse centroids of the HG-modes at different z_{k}, a Bayesian optimization routine is incorporated in the algorithm as an outer loop. The Bayesian optimization framework adopts a coarse-to-fine strategy, comprising a preliminary coarse search followed by a subsequent fine search. Typically, both stages are configured with 100 sampling evaluations, where each sample corresponds to 50 GS iterations. Consequently, the overall computational efficiency is dominated by the Bayesian optimization routine. In aggregate, this process entails cumulative 6000 to 10,000 iterations, corresponding to a computational time of approximately 15–20 min.

The phase distribution follows a prescribed initialization (not a random guess), as detailed in Ref. [69]. Consequently, the randomness of the algorithm originates from the random search path of the Bayesian optimization. We choose a high sampling density (∼200) to effectively suppress this randomness. As shown in Fig. 7, we take the measured Ti:sapphire laser intensity profiles in Fig. 6 as an example to illustrate the algorithm's reproducibility through six independent runs. The reconstructed phase profiles at the focal plane are the same across these runs, which demonstrates the robustness of the reconstruction method.

To further validate the phase retrieval algorithm, we examined two additional benchmark cases, one using an ideal Gaussian laser pulse and the other using a 785 nm solid-state laser. For the Gaussian laser case, we chose $w_0 = 25.9$ μm and numerically generated the intensity profiles at the focus and the −2 mm plane. The near-field intensity profile calculated using the retrieved phase achieved exceptional fidelity with the goal, yielding a SSIM of 0.99999976 and a PSNR of 85.92 dB only after 2 iterations. The 785 nm laser coaxially propagated with

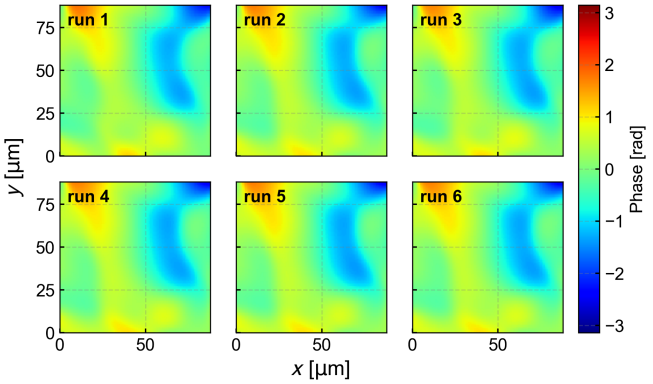


FIG. 7. The reconstructed phase profiles at the focal plane from six independent runs.

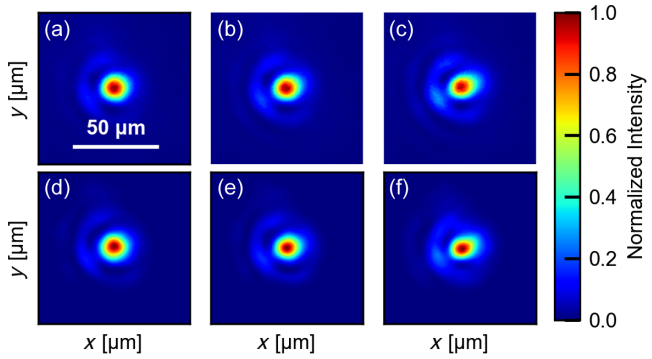


FIG. 8. GSA-MD results of a 785 nm solid-state laser. (a)–(c) depict the measured intensity profiles at 0, −100, and −250 μm, respectively. (d)–(f) are the retrieved intensity distributions at 0, −100, and −250 μm, respectively. Note that a pixel represents a physical size of 0.44 × 0.44 μm.

the laser pulse driver used in the LWFA experiments and exhibited high-quality flattop beam characteristics. We implemented the GSA-MD algorithm using intensity profiles in 3 planes: the focal plane, −100 μm, −250 μm, as shown in Fig. 8. With an increase in the number of intensity profiles, the algorithm can skip local minima effectively. We compared the calculated intensity profile in the −150 μm plane with the measured intensity and achieved a SSIM of 0.998 and a PSNR of 49.1 dB. Following the guidelines in Ref. [69]—namely using a high sampling density in the embedded Bayesian optimization and enforcing stringent convergence criteria—the phase retrieval algorithm produces consistent results across independent runs.

Zernike polynomials $Z_n^m(\rho,\theta)$ of the retrieved phase of the laser driver reveal the existence of low-amplitude, high-frequency noise, which is a known artifact of GS phase retrieval in low-intensity zones [72]. Thus, we implemented a Zernike-polynomials-based filter to eliminate $n > 12$ polynomials. We then calculated the propagation of the laser in vacuum using the AS diffraction code. As shown in Fig. 9(a), we observed coefficients $Z_1^{-1} = 0.173$ rad and $Z_1^1 = 0.246$ rad, corresponding to tilting components of the y and x directions, and a third-order aberration of $W_{11} = \sqrt{(Z_1^{-1} - 2Z_3^{-1})^2 + (Z_1^1 - 2Z_3^1)^2} = 0.809$ rad, which can lead to an obvious deflection. Due to the inhomogeneous intensity distribution and the presence of other aberrations, the deflection of the laser center is complex and does not follow a simple linear trend, as illustrated by the blue lines in Fig. 9(b). This large deviation in x direction would significantly increase the PIC simulation cost due to the demand for a wider simulation box and more azimuthal modes. To avoid this, we modified these two tilting terms to let the laser have the minimum deflection. As shown by the orange lines in Fig. 9(b), the maximum offset in both directions is less than 5 μm. The PIC simulations with a laser pulse with the modified terms also confirmed that the offset is small [red lines in (b)].

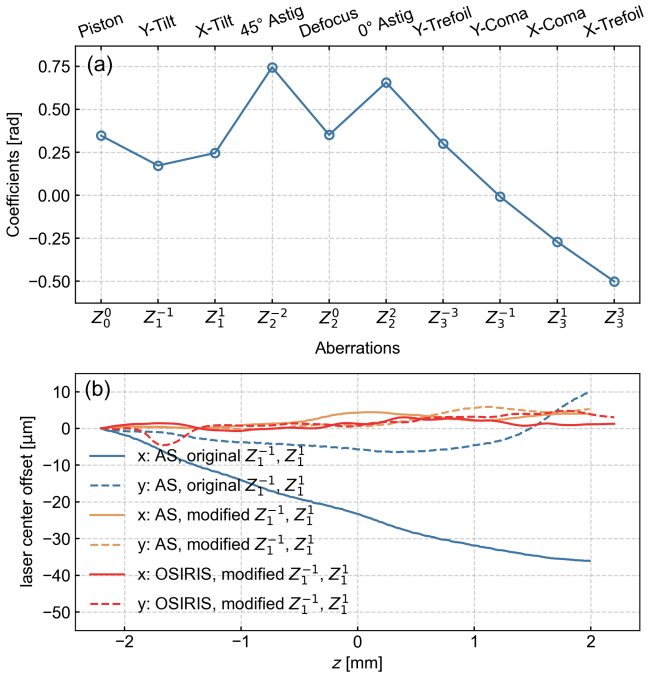


FIG. 9. (a) The first 10 Zernike polynomials of the realistic laser phase. (b) The deflection of the transverse center of the laser in vacuum calculated using the AS diffraction code with original Z_1^{-1} and Z_1^1 (blue lines), and with modified Z_1^{-1} and Z_1^1 (orange lines). The red lines are the results in plasma obtained from OSIRIS.

APPENDIX B: 3D ELECTROMAGNETIC FIELDS OF THE LASER PULSE

The 3D spatial distribution of the laser's EM fields needs to be initialized at the entrance of the plasma in PIC simulations. Since the focal plane is at 1.2 mm inside the plasma, the initial laser pulse is $0.46z_R$ away from the vacuum focus. We can use the AS diffraction code to obtain the complex amplitude of the laser central slice at the plasma entrance based on the reconstructed information at the focus.

By assuming a Gaussian temporal envelope, the intensity and phase distribution at other transverse planes can be expressed as

$$I(z,x,y) = I(z_n,x,y)\exp\left[-4\ln 2\frac{(z-z_n)^2}{(c\tau_{FWHM})^2}\right], \quad \text{(B1)}$$

$$\Phi(z,x,y) = k(z-z_n) + \Phi(z_n,x,y), \quad \text{(B2)}$$

where z_n is the center of the laser pulse, $I(z_n,x,y)$ and $\Phi(z_n,x,y)$ are the intensity and phase distributions measured or reconstructed in the experiments. Since the duration of the laser pulse is ∼30 fs, the radius of curvature of the wavefront and the difference of the Gouy phase over the ultrashort laser are not included in Eqs. (B1) and (B2). Furthermore, since the laser pulse considered here contains

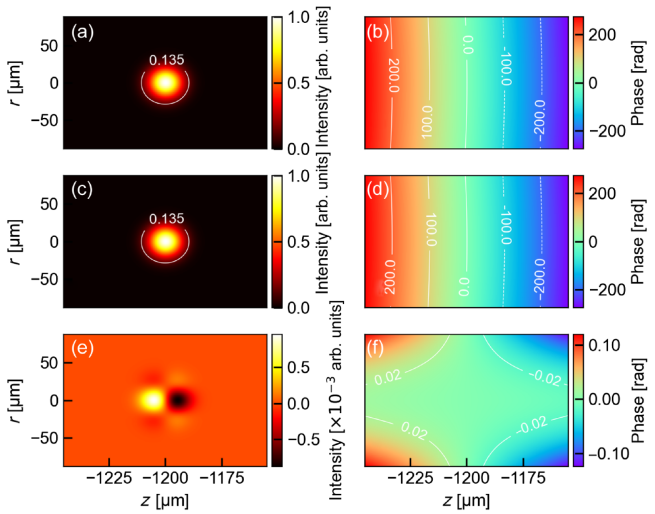


FIG. 10. Comparison between the formula [(a) for intensity and (b) for phase] and numerical results using Eqs. (B1) and (B2) [(c) for intensity and (d) for phase] for an ideal Gaussian laser, (e) shows the intensity difference between (a) and (c), and (f) shows the phase difference between (b) and (d).

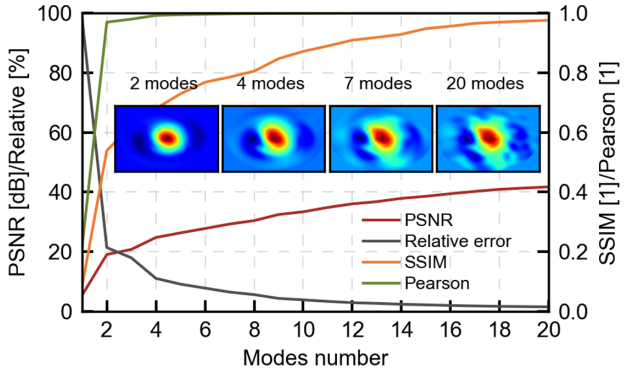


FIG. 11. The similarity between the realistic laser spot and the laser spot used as OSIRIS input with different numbers of modes. Gray line is relative error, orange line is SSIM, green line is Pearson correlation, and red line is PSNR. Insets are the reconstructed electric field slice with different numbers of modes.

several dozen cycles, the carrier-envelope phase does not play a critical role in the LWFA and it is chosen to let the peak of the envelope coincide with the peak of the fields. The EM fields of the laser pulse can be obtained straightforwardly from Eqs. (B1) and (B2).

The feasibility of constructing the 3D spatial distribution of the EM fields using the above assumption was demonstrated using the Gaussian laser pulse in case g. Figures 10(a) and 10(b) show the intensity and phase distributions calculated by the ideal Gaussian laser formula, while Figs. 10(c) and 10(d) display the corresponding distributions reconstructed using Eqs. (B1) and (B2) with the intensity and phase profiles at $z_n = -1.2$ mm. As shown in Figs. 10(e) and 10(f), the maximum intensity and phase differences are 9.6×10^{-4} and 0.12 rad, respectively, both of which are negligible.

APPENDIX C: Q3D OSIRIS SIMULATION CHECK

In the Q3D PIC code, all the physical quantities are decomposed into different azimuthal modes as $\exp(im\theta)$, where m is an integer and θ is the azimuthal angle. Two modes ($m = 0$ and $m = 1$) are sufficient to model LWFAs driven by laser pulses with Gaussian transverse profiles. For realistic laser pulses with complicated transverse intensity and phase distributions, more modes are required [73]. The computational complexity of Q3D simulations scales as $(2n_{\text{modes}} - 1) \times n_z \times n_r$, where n_{modes} is the number of modes used, n_z and n_r are the numbers of grid points along the z and r directions, respectively. Furthermore, the number of macroparticles per cell in the azimuthal direction is suggested to be $4(n_{\text{modes}} - 1)$ [56]. A large n_{modes} can model the realistic laser pulse more accurately but with a significantly increased computational cost. We first decomposed the initial 3D laser electric field as $\exp(im\theta)$ and then reconstructed the field using limited mode number. We compared the reconstructed field at the laser center with the original data and results are shown in Fig. 11. When $n_{\text{modes}} = 7$, it can accurately characterize the primary features of the laser spot with a PSNR exceeding 30 dB and a SSIM reaching 0.8. When $n_{\text{modes}} = 20$, high-fidelity results with a PSNR of 40 dB, a SSIM of 0.94, and a Pearson correlation coefficient of 0.99968 are achieved. After evaluating the trade-off between the computational cost and the accuracy, we chose $n_{\text{modes}} = 7$ in the simulations presented in the main body.

[1] T. Tajima and J. M. Dawson, Laser electron accelerator, Phys. Rev. Lett **43**, 267 (1979).
[2] J. Faure, Y. Glinec, A. Pukhov, S. Kiselev, S. Gordienko, E. Lefebvre, J.-P. Rousseau, F. Burgy, and V. Malka, A laser–plasma accelerator producing monoenergetic electron beams, Nature (London) **431**, 541 (2004).
[3] C. G. R. Geddes, C. Toth, J. van Tilborg, E. Esarey, C. B. Schroeder, D. Bruhwiler, C. Nieter, J. Cary, and W. P. Leemans, High-quality electron beams from a laser wakefield accelerator using plasma-channel guiding, Nature (London) **431**, 538 (2004).
[4] S. P. Mangles, C. Murphy, Z. Najmudin, A. G. R. Thomas, J. Collier, A. E. Dangor, E. Divall, P. Foster, J. Gallacher, C. Hooker *et al.*, Monoenergetic beams of relativistic electrons from intense laser–plasma interactions, Nature (London) **431**, 535 (2004).
[5] W. Leemans *et al.*, Gev electron beams from a centimetre-scale accelerator, Nat. Phys. **2**, 696 (2006).
[6] A. J. Gonsalves, K. Nakamura, J. Daniels, C. Benedetti, C. Pieronek, T. C. H. de Raadt, S. Steinke, J. H. Bin, S. S. Bulanov, J. van Tilborg *et al.*, Petawatt laser guiding and electron beam acceleration to 8 GeV in a laser-heated

capillary discharge waveguide, Phys. Rev. Lett. **122**, 084801 (2019).

[7] C. Aniculaesei, T. Ha, S. Yoffe, L. Labun, S. Milton, E. McCary, M. M. Spinks, H. J. Quevedo, O. Z. Labun, R. Sain *et al.*, The acceleration of a high-charge electron bunch to 10 GeV in a 10-cm nanoparticle-assisted wakefield accelerator, Matter Radiat. Extremes **9**, 014001 (2024).

[8] A. Picksley, J. Stackhouse, C. Benedetti, K. Nakamura, H. Tsai, R. Li, B. Miao, J. Shrock, E. Rockafellow, H. Milchberg *et al.*, Matched guiding and controlled injection in dark-current-free, 10-GeV-class, channel-guided laser-plasma accelerators, Phys. Rev. Lett. **133**, 255001 (2024).

[9] O. Lundh, J. Lim, C. Rechatin, L. Ammoura, A. Ben-Ismaïl, X. Davoine, G. Gallot, J.-P. Goddet, E. Lefebvre, V. Malka *et al.*, Few femtosecond, few kiloampere electron bunch produced by a laser–plasma accelerator, Nat. Phys. **7**, 219 (2011).

[10] A. Buck, M. Nicolai, K. Schmid, C. M. S. Sears, A. Sävert, J. M. Mikhailova, F. Krausz, M. C. Kaluza, and L. Veisz, Real-time observation of laser-driven electron acceleration, Nat. Phys. **7**, 543 (2011).

[11] A. H. Lumpkin, M. LaBerge, D. W. Rule, R. Zgadzaj, A. Hannasch, O. Zarini, B. Bowers, A. Irman, J. P. Couperus Cabadağ, A. Debus, A. Köhler, U. Schramm, and M. C. Downer, Coherent optical signatures of electron microbunching in laser-driven plasma accelerators, Phys. Rev. Lett. **125**, 014801 (2020).

[12] K. Huang, Z. Jin, N. Nakanii, T. Hosokai, and M. Kando, Electro-optic 3D snapshot of a laser wakefield accelerated kilo-ampere electron bunch, Light Sci. Appl. **13**, 84 (2024).

[13] M. LaBerge, B. Bowers, Y.-Y. Chang, J. Couperus Cabadağ, A. Debus, A. Hannasch, R. Pausch, S. Schöbel, J. Tiebel, P. Ufer *et al.*, Revealing the three-dimensional structure of microbunched plasma-wakefield-accelerated electron beams, Nat. Photonics **18**, 952 (2024).

[14] Y. Ma *et al.*, Single-shot reconstruction of electron beam longitudinal phase space in a laser wakefield accelerator, Phys. Rev. X **15**, 031062 (2025).

[15] W. Leemans, A. Gonsalves, H.-S. Mao, K. Nakamura, C. Benedetti, C. Schroeder, C. Tóth, J. Daniels, D. Mittelberger, S. Bulanov *et al.*, Multi-GeV electron beams from capillary-discharge-guided subpetawatt laser pulses in the self-trapping regime, Phys. Rev. Lett. **113**, 245002 (2014).

[16] Y. Ma, L. Chen, M. Li, Y. Li, J. Wang, M. Tao, Y. Han, J. Zhao, K. Huang, W. Yan *et al.*, Multiple quasi-monoenergetic electron beams from laser-wakefield acceleration with spatially structured laser pulse, Phys. Plasmas **22**, 083102 (2015).

[17] W. Wang, W. Li, J. Liu, Z. Zhang, R. Qi, C. Yu, J. Liu, M. Fang, Z. Qin, C. Wang *et al.*, High-brightness high-energy electron beams from a laser wakefield accelerator via energy chirp control, Phys. Rev. Lett. **117**, 124801 (2016).

[18] E. Esarey, C. B. Schroeder, and W. P. Leemans, Physics of laser-driven plasma-based electron accelerators, Rev. Mod. Phys. **81**, 1229 (2009).

[19] C. Joshi, S. Corde, and W. B. Mori, Perspectives on the generation of electron beams from plasma-based accelerators and their near and long term applications, Phys. Plasmas **27**, 070602 (2020).

[20] W. Wang, K. Feng, L. Ke, C. Yu, Y. Xu, R. Qi, Y. Chen, Z. Qin, Z. Zhang, M. Fang *et al.*, Free-electron lasing at 27 nanometres based on a laser wakefield accelerator, Nature (London) **595**, 516 (2021).

[21] M. Labat, J. C. Cabadağ, A. Ghaith, A. Irman, A. Berlioux, P. Berteaud, F. Blache, S. Bock, F. Bouvet, F. Briquez *et al.*, Seeded free-electron laser driven by a compact laser plasma accelerator, Nat. Photonics **17**, 150 (2023).

[22] S. K. Barber, F. Kohrell, C. E. Doss, K. Jensen, C. Berger, F. Isono, Z. Eisentraut, S. Schröder, A. J. Gonsalves, K. Nakamura *et al.*, Greater than 1000-fold gain in a free-electron laser driven by a laser-plasma accelerator with high reliability, Phys. Rev. Lett. **135**, 055001 (2025).

[23] S. Corde, K. Ta Phuoc, G. Lambert, R. Fitour, V. Malka, A. Rousse, A. Beck, and E. Lefebvre, Femtosecond x rays from laser-plasma accelerators, Rev. Mod. Phys. **85**, 1 (2013).

[24] H. Schwoerer, B. Liesfeld, H.-P. Schlenvoigt, K.-U. Amthor, and R. Sauerbrey, Thomson-backscattered x rays from laser-accelerated electrons, Phys. Rev. Lett. **96**, 014802 (2006).

[25] M. A. Bake, A. Tursun, A. Aimidula, and B. Xie, Two-stage γ ray emission via ultrahigh intensity laser pulse interaction with a laser wakefield accelerated electron beam, Plasma Sci. Technol. **22**, 105201 (2020).

[26] S. Fourmaux, S. Corde, K. T. Phuoc, P. Lassonde, G. Lebrun, S. Payeur, F. Martin, S. Sebban, V. Malka, A. Rousse *et al.*, Single shot phase contrast imaging using laser-produced betatron x-ray beams, Opt. Lett. **36**, 2426 (2011).

[27] J. M. Cole, D. R. Symes, N. C. Lopes, J. C. Wood, K. Poder, S. Alatabi, S. W. Botchway, P. S. Foster, S. Gratton, S. Johnson *et al.*, High-resolution μCT of a mouse embryo using a compact laser-driven x-ray betatron source, Proc. Natl. Acad. Sci. U.S.A. **115**, 6335 (2018).

[28] B. Kettle *et al.*, Single-shot multi-keV x-ray absorption spectroscopy using an ultrashort laser-wakefield accelerator source, Phys. Rev. Lett. **123**, 254801 (2019).

[29] D. Wu, H. Lan, J. Liu, H. Lu, J. Zhang, J. Lv, X. Wu, H. Zhang, Y. Xia, Q. He *et al.*, Ultra-short lifetime isomer studies from photonuclear reactions using laser-driven ultra-intense γ-ray, arXiv:2402.15187.

[30] M. Zeng and O. Tesileanu, High-flux electron beams from laser wakefield accelerators driven by petawatt lasers, Plasma Sci. Technol. **19**, 070502 (2017).

[31] C. McGuffey, T. Matsuoka, S. Kneip, W. Schumaker, F. Dollar, C. Zulick, V. Chvykov, G. Kalintchenko, V. Yanovsky, A. Maksimchuk *et al.*, Experimental laser wakefield acceleration scalings exceeding 100 TW, Phys. Plasmas **19**, 063113 (2012).

[32] Y. Li, D. Li, K. Huang, M. Tao, M. Li, J. Zhao, Y. Ma, X. Guo, J. Wang, M. Chen *et al.*, Generation of 20 kA electron beam from a laser wakefield accelerator, Phys. Plasmas **24**, 023108 (2017).

[33] J. Couperus, R. Pausch, A. Köhler, O. Zarini, J. Krämer, M. Garten, A. Huebl, R. Gebhardt, U. Helbig, S. Bock *et al.*, Demonstration of a beam loaded nanocoulomb-class laser wakefield accelerator, Nat. Commun. **8**, 487 (2017).

[34] J. Götzfried, A. Döpp, M. F. Gilljohann, F. M. Foerster, H. Ding, S. Schindler, G. Schilling, A. Buck, L. Veisz, and

S. Karsch, Physics of high-charge electron beams in laser-plasma wakefields, Phys. Rev. X **10**, 041015 (2020).

[35] J. Liu, H. Lu, H. Lu, H. Zhang, X. Wu, D. Wu, H. Lan, J. Zhang, J. Lv, Q. Ma *et al.*, Generation of 400 pC electron bunches in laser wakefield acceleration utilizing a structured plasma density profile, Phys. Plasmas **30**, 113103 (2023).

[36] J. Xu, L. Bae, M. Ezzat, H. T. Kim, J. M. Yang, S. H. Lee, J. W. Yoon, J. H. Sung, S. K. Lee, L. Ji *et al.*, Nanoparticle-insertion scheme to decouple electron injection from laser evolution in laser wakefield acceleration, Sci. Rep. **12**, 11128 (2022).

[37] G. Pariente, V. Gallet, A. Borot, O. Gobert, and F. Quéré, Space–time characterization of ultra-intense femtosecond laser beams, Nat. Photonics **10**, 547 (2016).

[38] B. Alonso, A. Döpp, and S. W. Jolly, Space–time characterization of ultrashort laser pulses: A perspective, APL Photonics **9**, 070901 (2024).

[39] S. Howard, J. Esslinger, N. Weiße, J. Schröder, C. Eberle, R. H. W. Wang, S. Karsch, P. Norreys, and A. Döpp, Single-shot spatiotemporal vector field measurements of petawatt laser pulses, Nat. Photonics **19**, 898 (2025).

[40] A. R. Maier, N. M. Delbos, T. Eichner, L. Hübner, S. Jalas, L. Jeppe, S. W. Jolly, M. Kirchen, V. Leroux, P. Messner *et al.*, Decoding sources of energy variability in a laser-plasma accelerator, Phys. Rev, X **10**, 031039 (2020).

[41] C. Berger, S. Barber, F. Isono, K. Jensen, J. Natal, A. Gonsalves, and J. van Tilborg, Active nonperturbative stabilization of the laser-plasma-accelerated electron beam source, Phys. Rev. Accel. Beams **26**, 032801 (2023).

[42] A. Amodio, D. Wang, C. Berger, H.-E. Tsai, S. K. Barber, J. van Tilborg, A. Picksley, Z. Eisentraut, N. R. Vora, M. Logantha, and etal and, Pointing stabilization of a 1 Hz high-power laser via machine learning, High Power Laser Sci. Eng. **13**, e35 (2025).

[43] K. Jensen, S. K. Barber, C. Berger, C. E. Doss, F. Kohrell, J. van Tilborg, S. J. Coleman, N. M. Cook, J. Edelen, and J. Einstein-Curtis, Improved laser-plasma accelerator stability via high-bandwidth longitudinal focal position stabilization of a 100 TW-class laser system, Phys. Rev. Accel. Beams **28**, 092802 (2025).

[44] S. Mangles, G. Genoud, S. Kneip, M. Burza, K. Cassou, B. Cros, N. Dover, C. Kamperidis, Z. Najmudin, A. Persson *et al.*, Controlling the spectrum of x-rays generated in a laser-plasma accelerator by tailoring the laser wavefront, Appl. Phys. Lett. **95**, 181106 (2009).

[45] B. Beaurepaire, A. Vernier, M. Bocoum, F. Böhle, A. Jullien, J. Rousseau, T. Lefrou, D. Douillet, G. Iaquaniello, R. Lopez-Martens *et al.*, Effect of the laser wave front in a laser-plasma accelerator, Phys. Rev. X **5**, 031012 (2015).

[46] Y. Glinec, J. Faure, A. Lifschitz, J. M. Vieira, R. A. Fonseca, L. O. Silva, and V. Malka, Direct observation of betatron oscillations in a laser-plasma electron accelerator, Europhys. Lett. **81**, 64001 (2008).

[47] S. Corde, C. Thaury, A. Lifschitz, G. Lambert, K. Ta Phuoc, X. Davoine, R. Lehe, D. Douillet, A. Rousse, and V. Malka, Observation of longitudinal and transverse self-injections in laser-plasma accelerators, Nat. Commun. **4**, 1 (2013).

[48] N. Nakanii, T. Hosokai, K. Iwasa, N. Pathak, S. Masuda, A. Zhidkov, H. Nakahara, N. Takeguchi, Y. Mizuta, T. Otsuka *et al.*, Effect of halo on the stability of electron bunches in laser wakefield acceleration, Europhys. Lett. **113**, 34002 (2016).

[49] J. Ferri, X. Davoine, S. Fourmaux, J. C. Kieffer, S. Corde, K. Ta Phuoc, and A. Lifschitz, Effect of experimental laser imperfections on laser wakefield acceleration and betatron source, Sci. Rep. **6**, 27846 (2016).

[50] Z.-H. He, B. Hou, V. Lebailly, J. A. Nees, K. Krushelnick, and A. G. R. Thomas, Coherent control of plasma dynamics, Nat. Commun. **6**, 7156 (2015).

[51] D. Oumbarek Espinos, A. Rondepierre, A. Zhidkov, N. Pathak, Z. Jin, K. Huang, N. Nakanii, I. Daito, M. Kando, and T. Hosokai, Notable improvements on LWFA through precise laser wavefront tuning, Sci. Rep. **13**, 18466 (2023).

[52] F. S. Tsung, R. Narang, W. B. Mori, C. Joshi, R. A. Fonseca, and L. O. Silva, Near-gev-energy laser-wakefield acceleration of self-injected electrons in a centimeter-scale plasma channel, Phys. Rev. Lett. **93**, 185002 (2004).

[53] S. Kalmykov, S. A. Yi, V. Khudik, and G. Shvets, Electron self-injection and trapping into an evolving plasma bubble, Phys. Rev. Lett. **103**, 135004 (2009).

[54] W. B. Mori, The physics of the nonlinear optics of plasmas at relativistic intensities for short-pulse lasers, IEEE J. Quantum Electron. **33**, 1942 (1997).

[55] W. Lu, M. Tzoufras, C. Joshi, F. S. Tsung, W. B. Mori, J. Vieira, R. A. Fonseca, and L. O. Silva, Generating multi-GeV electron bunches using single stage laser wakefield acceleration in a 3D nonlinear regime, Phys. Rev. ST Accel. Beams **10**, 061301 (2007).

[56] A. Davidson, A. Tableman, W. An, F. S. Tsung, W. Lu, J. Vieira, R. A. Fonseca, L. O. Silva, and W. B. Mori, Implementation of a hybrid particle code with a PIC description in r–z and a gridless description in ϕ into OSIRIS, J. Comput. Phys. **281**, 1063 (2015).

[57] R. A. Fonseca *et al.*, High performance computing in particle accelerator science and technology-OSIRIS: A three-dimensional, fully relativistic particle in cell code for modeling plasma based accelerators, Lect. Notes Comput. Sci. **2331**, 342 (2002).

[58] G.-Z. Sun, E. Ott, Y. C. Lee, and P. Guzdar, Self-focusing of short intense pulses in plasmas, Phys. Fluids **30**, 526 (1987).

[59] P. Sprangle, C.-M. Tang, and E. Esarey, Relativistic self-focusing of short-pulse radiation beams in plasmas, IEEE Trans. Plasma Sci. **15**, 145 (1987).

[60] X. Xu, T. N. Dalichaouch, J. Liu, Q. Ma, J. Pierce, K. Miller, X. Yan, and W. B. Mori, Generation of ultrabright and low energy spread electron beams in laser wakefield acceleration in a uniform plasma, Phys. Rev. Accel. Beams **26**, 111302 (2023).

[61] J. Wang, M. Zeng, D. Li, X. Wang, and J. Gao, High quality beam produced by tightly focused laser driven wakefield accelerators, Phys. Rev. Accel. Beams **26**, 091303 (2023).

[62] X. Xu, F. Li, W. An, T. Dalichaouch, P. Yu, W. Lu, C. Joshi, and W. Mori, High quality electron bunch generation using a longitudinal density-tailored plasma-based accelerator in

the three-dimensional blowout regime, Phys. Rev. Accel. Beams **20**, 111303 (2017).

[63] B. Sanyasi Rao, M. H. Cho, H. T. Kim, J. H. Shin, K. H. Oh, J. H. Jeon, B. J. Yoo, S. H. Cho, J. W. Yoon, J. H. Sung, S. K. Lee, and C. H. Nam, Optical shaping of plasma cavity for controlled laser wakefield acceleration, Phys. Rev. Res. **2**, 043319 (2020).

[64] T. N. Dalichaouch, X. L. Xu, A. Tableman, F. Li, F. S. Tsung, and W. B. Mori, A multi-sheath model for highly nonlinear plasma wakefields, Phys. Plasmas **28**, 063103 (2021).

[65] J. E. Shrock, E. Rockafellow, B. Miao, M. Le, R. C. Hollinger, S. Wang, A. J. Gonsalves, A. Picksley, J. J. Rocca, and H. M. Milchberg, Guided mode evolution and ionization injection in meter-scale multi-GeV laser wakefield accelerators, Phys. Rev. Lett. **133**, 045002 (2024).

[66] https://en.wikipedia.org/wiki/Pearson_correlation_coefficient.

[67] Y. Xia, Data and scripts for: Effects of realistic laser intensity and phase distribution on high-charge LWFA, GitHub 1.0.0 (2026), https://github.com/PKUxyh/2025-High-Charge.

[68] I. Moulanier, L. T. Dickson, C. Ballage, O. Vasilovici, A. Gremaud, S. Dobosz Dufrénoy, N. Delerue, L. Bernardi, A. Mahjoub, A. Cauchois, A. Specka, F. Massimo, G. Maynard, and B. Cros, Modeling of the driver transverse profile for laser wakefield electron acceleration at apollon research facility, Phys. Plasmas **30**, 053109 (2023).

[69] I. Moulanier, L. T. Dickson, F. Massimo, G. Maynard, and B. Cros, Fast laser field reconstruction method based on a Gerchberg–Saxton algorithm with mode decomposition, J. Opt. Soc. Am. B **40**, 2450 (2023).

[70] Z. Wang, A. Bovik, H. Sheikh, and E. Simoncelli, Image quality assessment: from error visibility to structural similarity, IEEE Trans. Image Process. **13**, 600 (2004).

[71] A. Horé and D. Ziou, Image quality metrics: PSNR vs SSIM, in *Proceedings of the 2010 20th International Conference on Pattern Recognition* (2010), pp. 2366–2369, https://ieeexplore.ieee.org/document/5596999/.

[72] J. R. Fienup, Phase retrieval algorithms: A comparison, Appl. Opt. **21**, 2758 (1982).

[73] I. Zemzemi, F. Massimo, and A. Beck, Azimuthal decomposition study of a realistic laser profile for efficient modeling of laser wakefield acceleration, J. Phys. Conf. Ser. **1596**, 012054 (2020).